



Mapping carbon nanotube orientation by fast fourier transform of scanning electron micrographs

Eileen Brandley^a, Emile S. Greenhalgh^a, Milo S.P. Shaffer^{b,*}, Qianqian Li^{a,**}

^a Department of Aeronautics, Imperial College London, London, United Kingdom

^b Department of Chemistry, Imperial College London, London, United Kingdom

ARTICLE INFO

Article history:

Received 1 December 2017

Received in revised form

15 April 2018

Accepted 21 April 2018

Available online 24 April 2018

ABSTRACT

A novel method of applying a two-dimensional Fourier transform (2D-FFT) to SEM was developed to map the CNT orientation in pre-formed arrays. Local 2D-FFTs were integrated azimuthally to determine an orientation distribution function and the associated Herman parameter. This approach provides data rapidly and over a wide range of lengthscales.

Although likely to be applicable to a wide range of anisotropic nanoscale structures, the method was specifically developed to study CNT veils, a system in which orientation critically controls mechanical properties. Using this system as a model, key parameters for the 2D-FFT analysis were optimised, including magnification and domain size; a model set of CNT veils were pre-strained to 5%, 10% and 15%, to vary the alignment degree. The algorithm confirmed a narrower orientation distribution function and increasing Herman parameter, with increasing pre-strain.

To validate the algorithm, the local orientation was compared to that derived from a common polarised Raman spectroscopy. Orientation maps of the Herman parameter, derived by both methods, showed good agreement. Quantitatively, the mean Herman parameter calculated using the polarised Raman spectroscopy was 0.42 ± 0.004 compared to 0.32 ± 0.002 for the 2D-FFT method, with a correlation coefficient of 0.73. Possible reasons for the modest and systematic discrepancy were discussed.

© 2018 The Authors. Published by Elsevier Ltd. This is an open access article under the CC BY license (<http://creativecommons.org/licenses/by/4.0/>).

1. Introduction

Over recent decades researchers have become aware of the potential to include carbon nanotubes (CNTs) in composites to create a new generation of composite structures with exceptional strength and stiffness, as well as improved thermal and electrical properties. However, in many cases, the observed performance is lower than expected, due in large part to the challenge of aligning high loading fractions of high quality, high aspect ratio CNTs [1–3]. One particularly promising approach relies on the impregnation of pre-formed CNT arrays, such as veils, ribbons and ropes, with a polymer matrix. Aligning carbon nanotubes within such preformed arrays can improve mechanical [4–7], thermal [8–11] and electrical [12–14] properties. A number of studies have shown an linear increase in tensile modulus and strength with an increase in orientation (Fig. 1).

* Corresponding author.

** Corresponding author.

E-mail addresses: m.shaffer@imperial.ac.uk (M.S.P. Shaffer), Qianqian.li@imperial.ac.uk (Q. Li).

CNTs in these preformed arrays can be orientated by plastic deformation either when dry or following infusion with a resin for lubrication and cohesion. Improved alignment applies the intrinsically excellent axial properties of the CNTs in a desired direction, as well as promoting higher loading fractions and improved van der Waals intertube interactions [4]. Since orientation has a large influence on the physical and mechanical properties of CNT veils and their composites, it is important to quantify the alignment accurately. In particular, it is interesting to map the degree of alignment across the structure to understand uniformity and localisation effects that may limit drawing. Quantified alignment helps to interpret performance, optimise processing, and can be implemented in computational models or empirical calculations of veil composites.

The alignment of an individual carbon nanotube can be defined by the Euler angles, θ , φ and ε as in Fig. 2 where θ is the polar angle of the CNT tube from the Z-axis of the veil, i.e. alignment direction, φ is the second rotation about X-axis and ε is the angle of rotation about the former Z-axis (now z' [20]). Within a veil, or other construct or composite, the orientation distribution function can be defined, $f(\theta, \varphi, \varepsilon)$. A spherical mapping is typically used to project

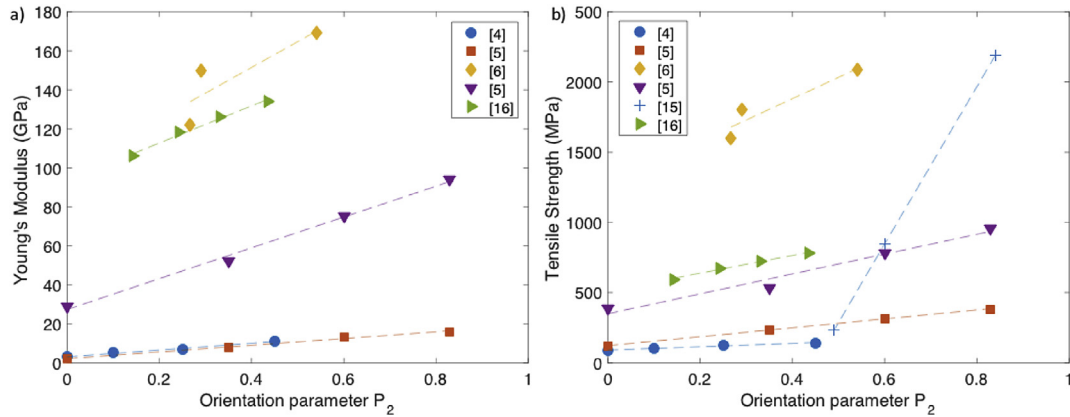


Fig. 1. Summary of current literature showing the relationship between the orientation parameter and (a) Tensile Strength and (b) Young's Modulus [4–6,15,16]. (A colour version of this figure can be viewed online.)

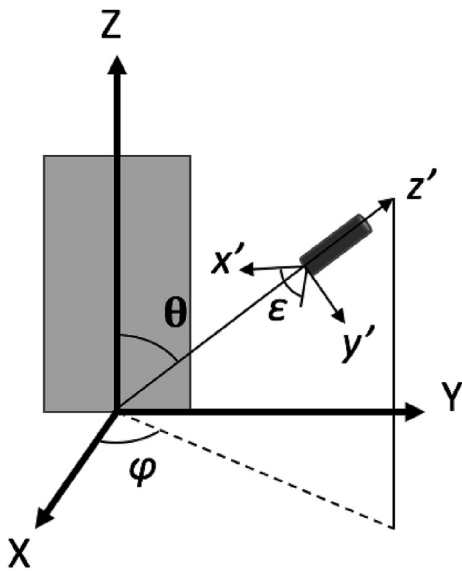


Fig. 2. Schematic of orientation of an individual carbon nanotube with respect to a CNT veil as described by the Euler angles θ , φ and ε .

these 3D spherical coordinates into a scalar value, such as the Herman's parameter in order to quantify the orientation between the nanotube and a defining axis.

The most common method used to measure CNT alignment is polarised Raman spectroscopy [17,18], using the two characteristics peaks, the D-band at 1350 cm^{-1} and the G-band at 1590 cm^{-1} [19]. The intensity of the G-band Raman scattering is sensitive to the orientation of carbon nanotubes when the excitation laser beam is linearly polarised. For an individual carbon nanotube, the polarised Raman intensity is proportional to $\cos^4 \beta$, where β is the angle between the polarised Raman direction and the carbon nanotube axis [20]. For an ideally aligned carbon nanotube, the polarised Raman intensity is a maximum when the incoming laser is polarised parallel to the nanotube direction, i.e. $\beta = 0^\circ$ and is a minimum when the polarisation is perpendicular i.e. $\beta = 90^\circ$. If all carbon nanotubes in the CNT veil are perfectly aligned, the Raman intensity is proportional to $\cos^4 \beta$. For carbon nanotubes that deviate from perfectly aligned nanotubes, Fischer proposed a detailed model to determine orientation [21]. Raman intensities measured at regular angles (between the polarised Raman direction and the CNT preferred axis, φ) can be fitted to an orientation distribution [5,21].

However, the majority of researchers have used a simple dichroic ratio Equation (1), for simplicity and ease of data collection:

$$R = \frac{A_{\parallel}}{A_{\perp}} \quad (1)$$

where R is the ratio between the Raman scattering parallel to the carbon nanotube direction and the Raman scattering perpendicular to the carbon nanotube direction. For highly aligned veils, in the parallel direction (\parallel), the ratio, R , tends to infinity and for highly aligned samples in the perpendicular direction (\perp) the ratio, R , tends to 0. For a sample with no overall alignment R is equal to 1. Although this ratio is widely used throughout literature, it only gives an indicative estimate of alignment [21]. One way to generate a more meaningful indication of alignment is to determine a general orientation parameter, also called the Herman parameter, S [22]. Although these methods were developed for single-walled nanotubes, similar behaviour been observed for multi-walled carbon nanotubes, since the diameters remain much smaller than the wavelength of the incident light [23].

In this work, uniaxial orientation is assumed, in such a case the orientation distribution function (ODF) is independent of φ and, since nanotubes are cylindrically symmetrical, the ODF is also independent of ε . For such a case, the ODF can be modelled as an expanded series of generalised spherical functions, the Legendre polynomial functions (Equations (2) and (3)) [20,24,25]:

$$f(\theta) = \sum_{i=1}^k \frac{2i+1}{2} \langle P_i(\cos \theta) \rangle P_i(\cos \theta) \quad (2)$$

$$\langle P_i(\cos \theta) \rangle = \int_0^\pi P_i(\cos \theta) d\theta \quad (3)$$

where $P_i(\cos \theta)$ is the Legendre polynomial. The average values of the Legendre polynomials are defined as orientation parameters where specifically $P_2(\cos \theta)$ is often termed the Herman's parameter. The limiting values of the Herman's parameter are $S = 1$ for perfectly aligned CNTs parallel to the major axis, $S = 0$ for systems where orientation is random and $S = -0.5$ for systems where the orientation is perfectly aligned perpendicular to the major axis.

The Herman's parameter for CNTs can be derived from measurements made at different polarisations. The usual configurations are: I_{VV} , incident polarisation and scattering polarisation parallel to the CNT axis; I_{VH} , incident polarisation parallel to the CNT axis and

perpendicular to the scattering polarisation; I_{HH} , incident polarisation and scattering polarisation perpendicular to the CNT axis. These intensities of each of these signals from a single nanotube is the function of the orientation (Equation (4) and Equation (5)) [20]:

$$I_{SWNT}^{VV} \propto [\cos \theta \cos \Phi - \sin \theta \sin \Phi \sin \varphi]^4 \quad (4)$$

$$I_{SWNT}^{VH} \propto [\cos \theta \cos \Phi - \sin \theta \sin \Phi \sin \varphi]^2 \times [\cos \theta \sin \Phi - \sin \theta \cos \Phi \sin \varphi]^2 \quad (5)$$

$$I_{SWNT}^{HH} \propto \left[\cos \left(\theta - \frac{\pi}{2} \right) \cos \Phi - \sin \left(\theta - \frac{\pi}{2} \right) \sin \Phi \sin \varphi \right]^4 \quad (6)$$

The signal of a carbon nanotube veil can be related to the intensities of individual CNTs, by summation (Equation (7)), for example:

$$I_{Veil}^{VV} = \frac{\int_0^{2\pi} \int_0^{2\pi} \int_0^\pi I_{CNT}^{VV} f(\theta) \sin \theta d\theta d\varphi d\epsilon}{\int_0^{2\pi} \int_0^{2\pi} \int_0^\pi f(\theta) \sin \theta d\theta d\varphi d\epsilon} \quad (7)$$

Analogous equations exist for I_{VH} and I_{HH} [20].

By substituting the uniaxial orientation distribution expanded to the fourth polynomial into Equation (7), and its analogous forms, the Herman's parameter can be obtained (Equation (8)) [22]:

$$S = \frac{3I_{VV} + 3I_{VH} - 4I_{HH}}{3I_{VV} + 12I_{VH} + 8I_{HH}} \quad (8)$$

Raman spectra are usually obtained from a laser spot diameter of approximately 1 μm , with an acquisition time on the order of 10 s or more. Raman point spectra can be collected systematically to produce a large orientation map; however, acquiring a large map typically takes several hours. Whilst an optical microscopy image of the sample can be correlated with the map, the optical resolution limits the ability to correlate the observed spectra with specific structural arrangements of nanoscale objects.

Despite the vast range of electron micrographs of CNT veils and arrays, routinely used to examine the structures qualitatively, the alignment is rarely quantified. However, in other research areas, Fourier transforms are often used to analyse microscope images. One particularly relevant example is the use of fast Fourier transforms (2D-FFT) to measure fibre misalignment in conventional carbon fibre composites (fibre diameter on the order of 7 μm) [26]. On a smaller scale, 2D-FFT methods have been successfully applied to determine the alignment of electrospun scaffolds [27] and analyse elastin networks [28]. Using these examples as inspiration, a method was developed to measure the orientation of CNT veils, via image processing of electron micrographs via 2D-FFT. In particular, the methodology in this paper uses a similar algorithm to that applied to carbon fibre composites in Ref. [26] for performing a 2D-FFT but is developed further to calculate orientation parameters from the scanning electron micrographs. This paper presents the development and evaluation of this method, parameter optimisation for the algorithm, and the validation of the method by comparison to Raman results, for initial application to neat CNT veils.

2. Experimental

CNT veils were kindly provided by Suzhou Institute of Nano-Tech and Nano-Bionics (Chinese Academy of Sciences) and used as received. The CNTs in the veil were multiwalled CNTs with a diameter of approximately 10–30 nm, 10–15% iron catalyst, and

density 0.5 g/cm³. The veils were produced from vertically aligned CNT forests that had been directly grown on a predeposited catalyst film. The thickness of the veil sheet was measured to be 20 μm using a micrometer (Mitutoyo, MDC Lite Digital Micrometer). The CNT diameter was measured from scanning electron micrographs at a magnification of 100,000 (resolution of approximately 1 pixel per 7 nm). 100 CNTs diameters were measured with the average diameter of 16 nm and a standard deviation of 4.5 nm. Additional TEM images have been collected and included in [electronic supplementary information ESI-Fig. 1](#). The results were consistent with the SEM measurement.

CNT veils were mechanically stretched prior to imaging to achieve permanent deformation and thus vary the alignment. In order to prevent stress concentrations in the veil, the ends of the veils were bound to strips of silicone using double sided adhesive tape and clamped for testing. The mechanical stretching was conducted using an Instron 4505 screw driven machine at a stroke of 0.1 mm min⁻¹. 100 mm lengths of veil were stretched to engineering strain levels of 5%, 10% and 15%, as measured via a video gauge. After stretching, the clamped regions were cut from the sample and discarded.

The CNT veils were imaged via scanning electron microscopy (SEM) using a LEO Gemini 1525 FEG SEM (Carl Zeiss). The stretched samples for SEM imaging were mounted on aluminium stubs using silver paint to bind the sample to the stub (all Agar Scientific) and to reduce charging. The secondary electron detector was used to collect images at an accelerating voltage of 5 kV, working distance 5–10 mm.

SEM imaging of large areas was carried out by acquiring 12 \times 8 overlapping images. The ImageJ plugin MosaicJ [29] was used to stitch the images to obtain a single high resolution image of a 220 $\mu\text{m} \times 90 \mu\text{m}$ area of the veil. For domain size parameter optimisation, the large image was split into square domains of side length 20 μm , 10 μm , 5 μm , 2.5 μm and 1.25 μm for analysis. For producing an orientation map via 2D-FFT, the high-resolution image was split into domains of the order of 5 $\mu\text{m} \times 5 \mu\text{m}$, which were processed by the 2D-FFT algorithm. Image processing of the electron micrographs and the 2D-FFT algorithm were carried out via Matlab using several inbuilt Matlab functions explained in detail in Section 3 in this paper. For parameter optimisation, five random areas on the veil were imaged at nine different magnifications: 5.0 k, 10.0 k, 20.0 k, 30.0 k, 40.0 k, 50.0 k, 60.0 k, 70.0 k, 80.0 k.

Raman mapping was applied to the same region imaged in the SEM by applying a mask to the sample. The mask aided in the locating of the region of interest in both the SEM and Raman and ensuring identical regions were imaged in both methods. The mask was deposited by sputter-coating the sample with chromium, leaving only the region of interest exposed for mapping. Raman spectroscopy experiments were performed on a Renishaw inVia microRaman spectrometer with a 633 nm laser. A step size of 5 μm was used and an integration time of 10 s per step. For analysis, the G-Peak in the Raman spectrum was fitted with a mixed Gaussian-Lorentzian distribution to determine the peak height.

Raman orientation maps were generated with the Streamline image acquisition tool, using the 'slalom' function to ensure the complete coverage of the CNT veil within the designated region. Raman spectra were processed with both WiRE 4.1 software and Matlab. The CNT orientation was calculated by collecting polarised spectra, and applying Equation (8). The incident laser light was polarised by applying a half wave plate prior to interaction with the sample and analyser. Three polarisation configurations were applied: VV (incident and scattering light polarised parallel to the sample axis), VH (incident light polarised parallel to the sample axis and scattered light is polarised perpendicular to the sample axis)

and HH (incident light and scattered light polarised perpendicular to the sample axis) to measure the Raman intensity parallel and perpendicular, respectively, to the strain direction of the CNTs in the veil.

3. Fast Fourier transform methodology

The Fourier transform picks out repetitive elements in the original spatial domain image, and manifests them in the frequency domain [30]. In this case, the diameters of individual and bundled CNTs are the features of interest. The 2D-Fourier transform was computed using the inbuilt Matlab function FFT2, which returns the two-dimensional discrete Fourier transform (DFT) of the image. The DFT was computed with a fast Fourier transform (FFT) algorithm. The result of the transformation was a matrix of the same size as the original image [31]. The resulting information was in the frequency domain denoted. $F(u, v)$.

The 2D-Fourier transform is defined as:

$$F(u, v) = \int_{-\infty}^{\infty} \int_{-\infty}^{\infty} f(x, y) e^{-i2\pi(ux+vy)} dx dy \quad (9)$$

where x and y are the spatial domain dimensions and u and v are the spatial frequencies. In general, the solution to the 2D-FFT is complex;

$$F(u, v) = F_R(u, v) + iF_I(u, v) \quad (10)$$

where the subscript R and I indicate the real and imaginary parts of the solution respectively. To interpret the FFT, the magnitude at each pixel can be calculated, to give the power spectrum. The power spectrum contains no phase information but provides the total amount of information at a given frequency. The power spectrum is computed by:

$$|F(u, v)| = \left(F_R(u, v)^2 + F_I(u, v)^2 \right)^{\frac{1}{2}} \quad (11)$$

$$F_{\ln}(u, v) = \ln(1 + |F(u, v)|) \quad (12)$$

The dynamic range of the power spectrum is often mapped to an 8-bit greyscale using logarithmic transformation [26]:

The output of the above Matlab functions were translated to centre (zero-frequency component) [32] using the Matlab fftshift function, to simplify visualisation.

The mean fibre direction and orientation distribution function were calculated from the 2D-FFT power spectrum (see Fig. 3). In the 2D-FFT power spectrum (Fig. 3b), the azimuthal distribution of intensity relates to the orientations of the contributing CNTs (Fig. 3a). The total intensity for each angle θ was calculated by summing the intensity radially (shown as r in Fig. 3c and Equation (13)):

$$I_{\text{sum}}(\theta) = \sum F_{\ln}(r) \quad (13)$$

The azimuthal summation was performed across the whole FFT. It could be argued that the radial range should be selected to focus on the lengthscale of individual CNTs. However, it was found that the result was not significantly changed by introducing radial filtering ranges. The most likely explanation is that the short lengthscale detail is already averaged out by the magnification selected (see section 4.1). It is more efficient to collect only the data required rather than discard it digitally later.

To calculate the orientation distribution function, the summed intensity was fitted to a function (Equation (14)) based on a normal

distribution. The angle at which this orientation distribution function reached a maximum was interpreted as the local mean CNT direction, or director.

$$I(\theta) = a \exp\left(-\frac{(\theta - \mu)^2}{b^2}\right) + c \quad (14)$$

where μ is the predominant direction. The inbuilt Matlab function 'fit' was used to determine the coefficients a , b , and c , and hence obtain the orientation distribution function (ODF) (Fig. 3d). To compare different samples, the orientation distribution function was normalised (the normalised orientation distribution function, NODF) so that the integral over the range $0-\pi$ was one.

Finally, this normalised orientation distribution was converted into the Herman's parameter, S , using Equation (15), which represents the P_2 term in Equation (3), and Equation (16);

$$S = \frac{3 \cos^2 \theta - 1}{2} \quad (15)$$

where

$$\cos^2 \theta = \frac{\int_0^\pi I(\theta) \cos^2 \theta \sin \theta d\theta}{\int_0^\pi I(\theta) \sin \theta d\theta} \quad (16)$$

where $I(\theta)$ is the intensity of the orientation distribution function as shown in Equation (14).

4. Results and discussion

The CNT veils were readily imaged by FEG-SEM, without additional coating, allowing the underlying structure to be visualised at a range of resolutions. The approach described above, and summarised in Fig. 3, was used successfully to calculate the local order parameters. These CNT arrays were used as a case study in order to identify the best imaging magnification and domain size for the analysis.

4.1. Parameter optimisation

The sample contains structure at different characteristic lengthscales and the objects resolved at different magnifications may vary (for example, individual CNTs, bundles, particles, kinks, etc). Therefore the magnification at which the image data are collected can intrinsically affect the output of the algorithm, and has practical implications. The magnification sets the level of detail available within the image. In the context of composites, fibre alignment is the critical parameter and is therefore important to use sufficient magnification to resolve individual CNTs. On the other hand, at higher magnifications, details of the internal structure or surface of the CNTs can become visible, and potentially add noise to the desired ODF. Whilst higher resolution details could be filtered out digitally, it is quicker and more stable to use the minimum magnification required.

To explore the effects of magnification, five independent regions of a model veil were imaged at nine different magnifications (5.0 k, 10.0 k, 20.0 k, 30.0 k, 40.0 k, 50.0 k, 60.0 k, 70.0 k, 80.0 k which translates as approximately 0.4, 0.8, 1.6, 2.3, 3.1, 3.9, 4.7, 5.5, 6.2 pixels per CNT diameter respectively). For each region and magnification, identical domains in the micrograph were located and cropped (Fig. 4).

For the analysis, the magnifications were converted to a dimensionless measure, pixels per average CNT diameter, to

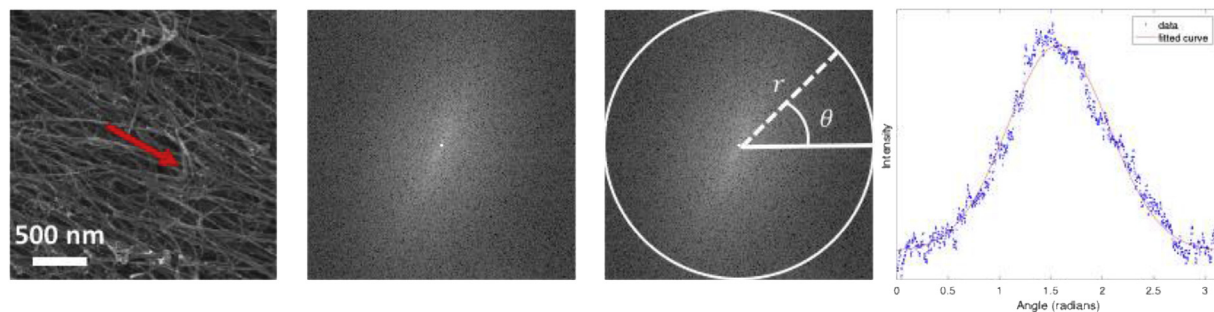


Fig. 3. Example showing the processing sequence used to determine the local orientation: a) Cropped SEM Image, arrow shows straining direction (15% strained sample, at a magnification of $\times 40.0$ k) b) FFT power spectrum c) azimuthal summation, (the summation is over the range $100 \mu\text{m}^{-1}$ to $0.2 \mu\text{m}^{-1}$) d) final orientation distribution function. (A colour version of this figure can be viewed online.)

simplify comparison to other systems in the future. The 2D-FFT was calculated for each image, and the orientation distribution function was computed from the 2D-FFT. Since the orientation intrinsically varies across the veil, the results from the independent regions were compared by the calculated Herman's parameter along with the coefficient of best fit for the resulting ODF (Fig. 5a). The most accurate magnification range has the lowest spread in the Herman parameter, which also coincides with the greatest coefficient of best fit.

At low magnifications (<1 pixel/CNT), the Herman's parameter varied significantly (Fig. 5a), and had a low associated coefficient of best fit (Fig. 5b.), as the individual CNTs are not sufficiently

resolved. At resolutions of 1–3 pixels/CNT (green region in Fig. 5) the normalised Herman's parameter falls consistently in a narrow range. As the resolution increased further, the range of Herman parameters again broadened, due to the additional detail in the image (such as CNT surface texture, contaminating nanoparticles, or simply imaging noise) unrelated to the primary CNT orientation. Therefore, for all further analysis in this paper, a magnification of 1–3 pixels/CNT was used. A similar effect might be obtained by applying a radial filter to the FFT of high resolution images before azimuthal integration. However, it is more efficient to collect only the necessary data rather than discarding information digitally. Within the selected magnification range, further radial filtering had little effect. The selected magnification (and implied frequency range) effectively evaluates the waviness of the CNTs due to deformation or growth stresses (typically on lengthscales of 100 nm or more) which is particularly relevant to the composite performance. Crystalline 'quality' of the CNTs which governs intrinsic axial properties, is better assessed by Raman spectroscopy, high resolution TEM, or other established methods [19]. Our TEM measurement (ESI-Figs. 1 and 2) has confirmed the general crystalline structure of the CNT veil used in this research with a low incidence of particles and kinks.

Next, the domain size used for mapping the alignment was considered. The size of this domain, of course, determines the resolution of the resulting orientation map. The Fourier Transform is a linear transform. That is, if there are two functions denoted $x(t)$ and $y(t)$ and their respective Fourier transforms, $F[x(t)]$ and $F[y(t)]$, then the Fourier Transform of any linear combination of $x(t)$ and $h(t)$ can be found. As is the case with one-dimensional Fourier Transforms, linearity applies to two dimensional transforms (Equation (17)) [33].

$$F\{a_1 f_1(x, y) + a_2 f_2(x, y)\} = a_1 F\{f_1(x, y)\} + a_2 F\{f_2(x, y)\} \quad (17)$$

Hence, any domain should be able to be split into smaller domains and the sum of the Fourier Transforms of the smaller domains should equal the Fourier transform of the large domain. From this perspective, it is expected that the Herman parameter of a given area should be independent of the domain size and number of domains used to calculate it. However the fitting algorithm may be challenged at smaller sample areas. To explore these aspects, a high definition stitched SEM image was split into six different square domain sizes of approximately; $20 \mu\text{m}$ (one domain), $10 \mu\text{m}$ (four domains), $6.7 \mu\text{m}$ (nine domains), $5 \mu\text{m}$ (sixteen domains), $2.5 \mu\text{m}$ (sixty four domains) and $1.2 \mu\text{m}$ (two hundred and sixty five domains) (Fig. 6a).

At small domain sizes, the spread of calculated Herman's parameters is large and the coefficient of best fit, R^2 , for fitting the 2D-FFT data to a Gaussian fit is poor (Fig. 6b and c). Small domains only

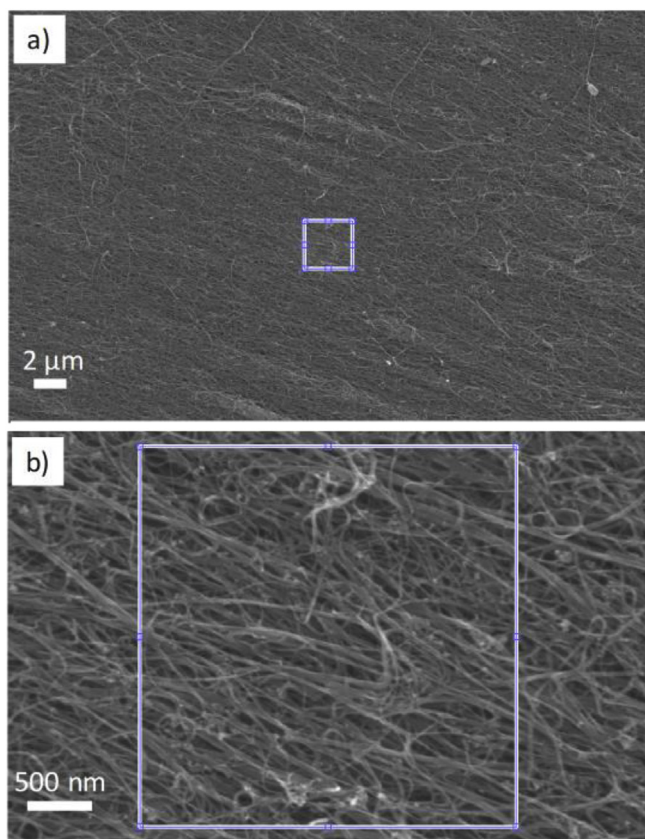


Fig. 4. Locating an identical area within SEM micrographs, a) image magnified to $\times 10.0$ k and b) image magnified to $\times 80.0$ k. The enclosed area in both images is identical. Model veil strained to 10%. (A colour version of this figure can be viewed online.)

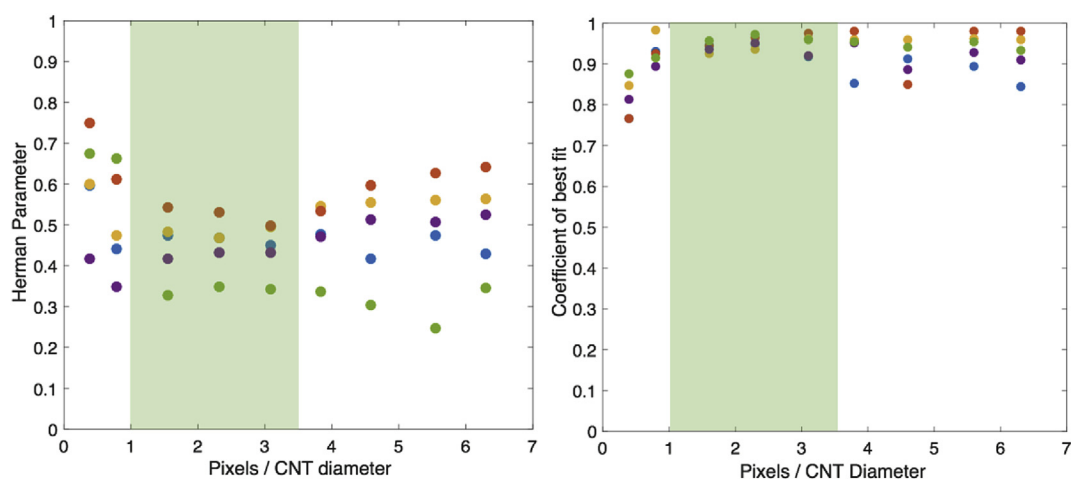


Fig. 5. a) Herman parameter as a function of image resolution for sample strained to 10%. b) Goodness of best fit, R^2 , value for the Gaussian fit of the azimuthal 2D-FFT data. The green area shows the optimum range of resolution for performing the analysis. (A colour version of this figure can be viewed online.)

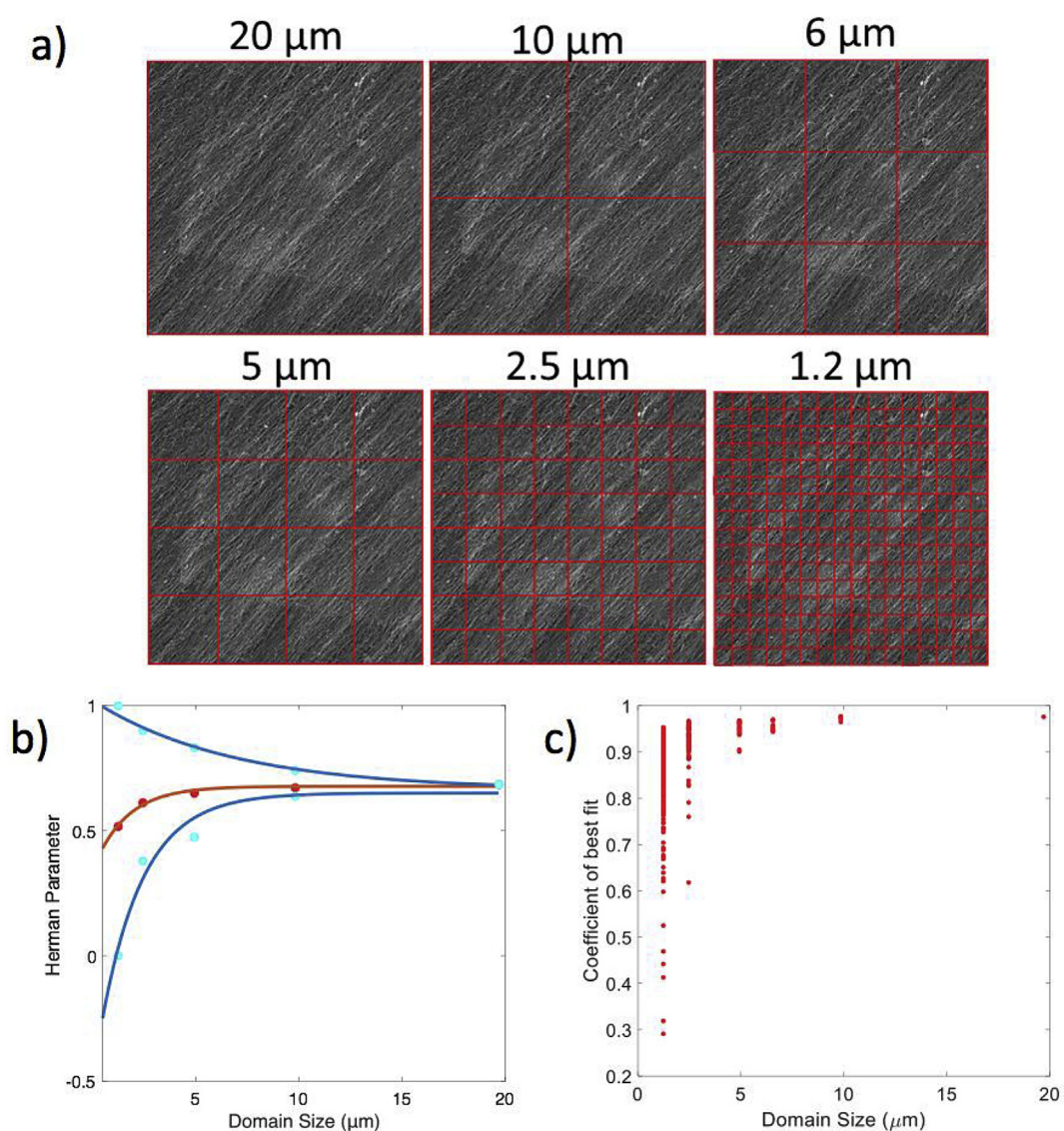


Fig. 6. a) Domains used in the analysis (veil strained to 10%). b) Plot of the minimum and maximum Herman parameter (blue lines) and the mean Herman parameter for each domain size. c) Plot of the coefficient of best fit for each domain size. (A colour version of this figure can be viewed online.)

encompass a small number of CNTs which reduces the statistical reliability of the fit. As the dimensions of the domain increase, more CNTs are sampled and the ODF fits the Gaussian model more reliably. The coefficient of best fit was deemed sufficiently high (>0.9) for domain sizes above $5\text{ }\mu\text{m}$, or approximately 160 CNT diameters, and this size was used for subsequent analysis.

4.2. CNT veil orientation measurement and validation

It has been shown previously, via polarised Raman spectroscopy, that straining veils induces CNT alignment [1,5]. Indeed, qualitatively, SEM (Fig. 7a–c) confirms increasing alignment with increasing applied strain (5%, 10% and 15%). In this study, it was not possible to apply strains greater than $\sim 15\%$ without breaking the veils. Higher strains have been reported using a variety of methods [4,18], but the maximum is likely dependent on the initial orientation of the veil, and other processing factors such as rate and lubrication. Here, different strains are applied simply to demonstrate the analysis method, although in the medium term, the approach should help to optimise the drawing process.

Therefore, it is expected that the veils strained to 5%, 10% and 15% would have increasing degrees of alignment, as indeed can be seen qualitatively in the electron micrographs (Fig. 7a–c). The alignment is characterised in the 2D-FFT, and therefore the computed orientation distribution function.

The orientation of the CNTs creates a repetitive pattern in the SEM micrograph perpendicular to the main CNT direction which becomes progressively more obvious as an anisotropic distribution in the 2D-FFT (Fig. 7). Using the optimised magnification and domain size, the orientation distribution function and Herman's parameters were calculated for each sample (Fig. 8). The resulting normalised orientation distribution functions computed from each 2D-FFT were narrower for the CNT veils with increasing strain. The original zero strain sample already has some orientation due to the original drawing process used to form the veil. The Herman's parameter was shown to increase with increasing applied strain as expected, due to the plastic deformation of the CNT veils under load [4].

For validation, the 2D-FFT method was compared to the more conventional polarised Raman spectroscopy approach, over a large area; an orientation map of a 10% strained CNT veil was created

over an identical region ($75 \times 90\text{ }\mu\text{m}^2$, Fig. 9), using both methods. For the 2D-FFT method, this mosaic image was split into domains of the order of $5\text{ }\mu\text{m} \times 5\text{ }\mu\text{m}$, and processed to obtain the primary director and Herman's parameter for each. For Raman spectroscopy, maps were obtained using HH, HV, and VV polarisations and a step size of $5\text{ }\mu\text{m}$, in order to calculate the Herman's parameters at each location, using Equation (7).

Both methods (Fig. 10-a and 10-b) produce qualitatively similar maps. For example, the area of high alignment was detected running diagonally across both the 2D-FFT and Raman orientation map, circled red. The mean Herman parameters were 0.32 ± 0.078 and 0.42 ± 0.080 when calculated via 2D-FFT and polarised Raman, respectively. There is, therefore, a reasonable match between these mean values, where the error is the standard deviation of all the domains in the map. However, as can be seen from the histograms, the 2D-FFT method calculated a broader range of Herman parameters as compared to the polarised Raman methodology. In fact, the coefficient of correlation, i.e. the degree to which two variables are related, between the two orientation maps is 0.73. The differences in the orientation maps could have various origins, including a difference in mathematical definition or varying penetration depths.

The experimental differences between scanning electron microscopy and Raman spectroscopy may explain some of the differences between the maps. Scanning electron microscopy is generally considered a surface technique [34] therefore the depth of analysis is likely to be lower than that of Raman. From high magnification SEM micrographs (Fig. 11) approximately 5 layers of nanotubes from the veil are imaged, indicating a penetration depth of approximately 150 nm (estimated based on a nanotube diameter of 10 nm and volume fraction of 0.3). In comparison to SEM, Raman penetrates deeper [35], with reported penetration depth up to 30 of layers for graphene [36]. Notably, there are dark regions in the SEM from which no secondary electrons are collected, however, these regions likely still contribute to the Raman signal. If the CNT veils are not homogenous in orientation through the thickness of the veils, these penetration depths will lead to differences in the calculated Herman's parameter.

More fundamentally, the FFT is sensitive to the topology of the CNTs, as revealed by the secondary electron generation. Raman is sensitive to local polarisability and crystallinity. Therefore,

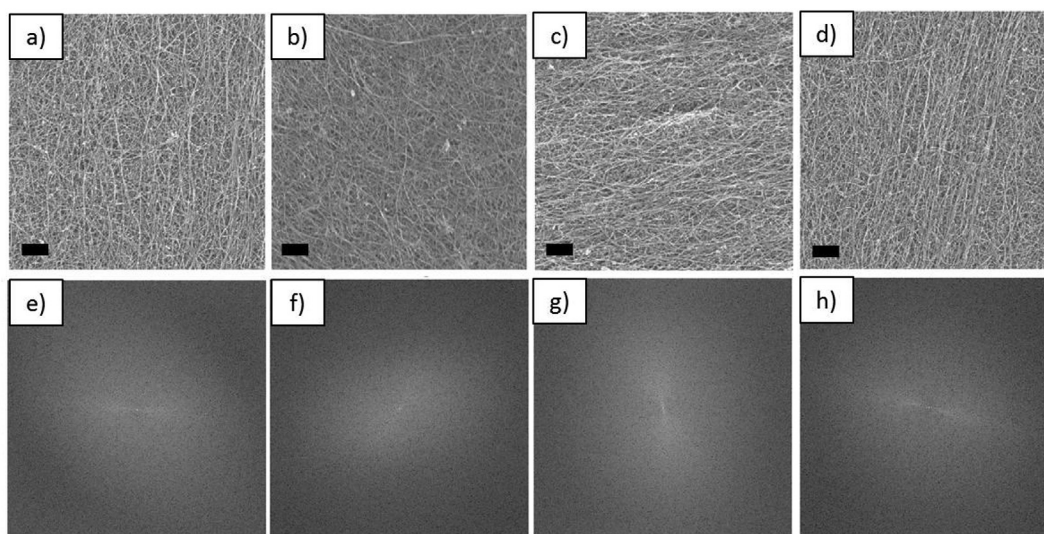


Fig. 7. SEM image (a–d) and associated 2-D FFT (e–h) for (a, e) 0% strained, (b, f) 5% strained and (c, g) 10% strained CNT veils, (d, h) 15% strained CNT veils. The scale bar on the micrographs indicates 500 nm and azimuthal integration of the 2D-FFT is over the range $50\text{ }\mu\text{m}^{-1}$ to $0.4\text{ }\mu\text{m}^{-1}$.

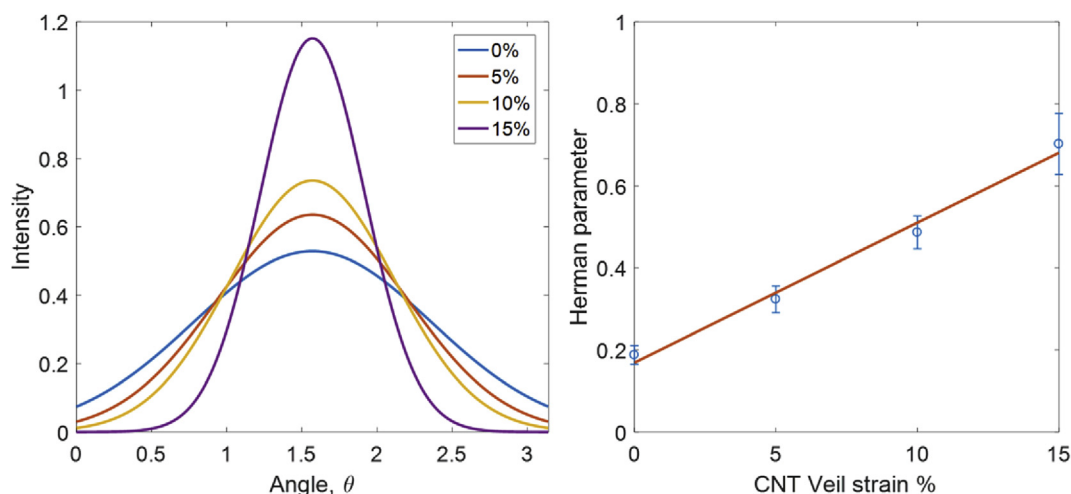


Fig. 8. (a) Orientation distribution function for CNT veil aligned as a function of applied strain. (b) Calculated average Herman's parameter for each of the CNT samples (analysed at a resolution of 2 pixels/CNT diameter and a square domain of $5\ \mu\text{m} \times 5\ \mu\text{m}$). (A colour version of this figure can be viewed online.)

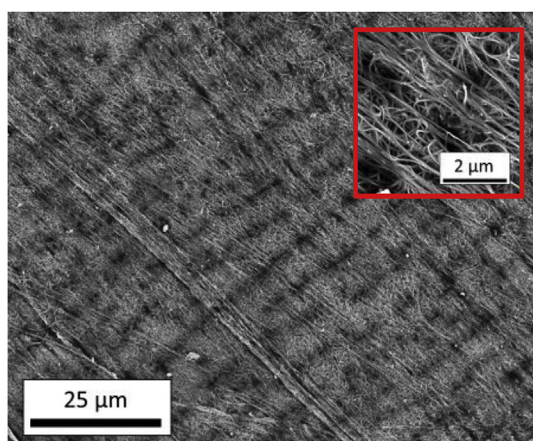


Fig. 9. Mosaic image of a large high resolution area of CNT veil, assembled from individual SEM images stitched together. Inset is an example of one of the individual $5\ \mu\text{m}$ domains for used in creating the image. (A colour version of this figure can be viewed online.)

differences in crystallinity will affect the signals differently. Disruption to the crystalline quality of the CNTs or the orientation of the graphitic planes to the CNT axis will reduce the degree of orientation measured by Raman spectroscopy; however, the FFT will only be affected if there is gross distortion of the CNT shape. On the other hand, the FFT-based Herman's parameter will be more strongly reduced by CNT ends/discontinuities, and features related to intersecting CNTs, as well as lost information from unresolved parallel bundles. Since these CNT samples are relatively crystalline (I_G/I_D ratio of a sample area of pristine CNT veils varies from 8.2 to 13.6 (example spectre, ESI-Fig. 4)), and the Raman-derived Herman's parameter is higher, it seems likely that these latter effects may be the dominant source of divergence.

5. Conclusions

A novel method was developed to quantify the alignment of carbon nanotubes within pre-formed arrays, specifically including veils. By taking a 2D fast Fourier transform of a scanning electron micrograph, the local orientation was converted into an ODF and

subsequently into a Herman's orientation parameter. The most effective magnification for this analysis was found to be around 1–3 pixel/CNT diameter, in order to resolve the principle features related to overall orientation. In addition, to successfully extract a statistically meaningful single director, a minimum region size of 200–500 CNT diameters was required, defining the resolution limit of the resulting orientation maps.

By quantifying orientation via image processing techniques, large scale high resolution orientation maps can be produced at much faster rates than current techniques. Such maps can resolve orientational inhomogeneities which are in good qualitative agreement with orientation maps created using more common polarised Raman spectroscopy. Small deviations in the absolute Herman parameter extracted from the two methods may reflect the fundamental differences between the techniques. It is not immediately obvious which absolute measurement is more relevant to the development of practical applications of such veils. Both approaches assume approximately planar arrangements; further refinement would be required to model more 3D distributions.

Nevertheless, the 2D-FFT approach offers a significant advantage in speed as compared to Raman mapping methods. Large Raman maps of the type used in this study can easily take more than 12 h to acquire, compared to less than an hour for stitched SEM images of a similar region, at the required resolution. The 2D-FFT method offers a simple, and easily understood, method to calculate the orientation of carbon nanotubes in pre-formed arrays, whilst directly observing the associated microstructural features. This type of information will assist the development of CNT orientation process and the associated performance of the resulting composites.

Whilst illustrated here for CNT veils, the methodology should be widely applicable to other nanostructured systems. The dimensionless magnification and domain size guidelines should provide a useful reference in such cases. The approach is directly applicable to CNT veil composites for which analysing and optimising the orientation of veils, as produced, before infusion is a key step for enhancing performance. In principle the method may also be directly applicable to CNT veil composites impregnated with a beam stable resin, since voltage contrast is observed from 'buried' CNTs; if necessary, plasma etching or other surface preparation could be used to enhance the CNT contrast [37, 38]. The method could also be applied to other CNT samples, related nanomaterials,

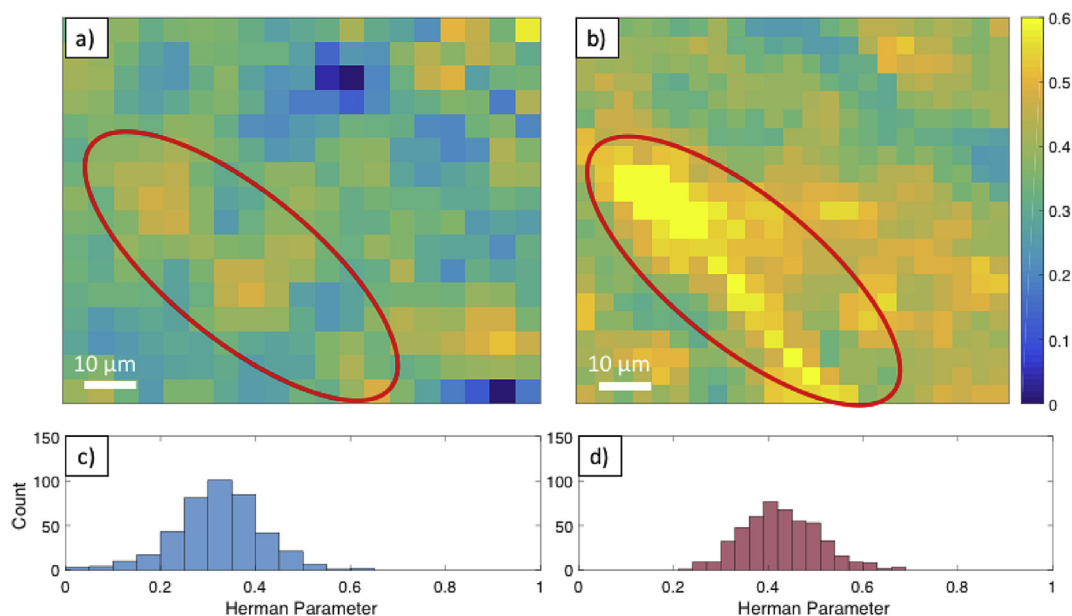


Fig. 10. Map of Herman parameters for the sample shown in Fig. 7, calculated using (a) 2D-FFT and (b) polarised Raman. Histogram of the Herman parameter for (c) 2D-FFT and (d) polarised Raman. (A colour version of this figure can be viewed online.)

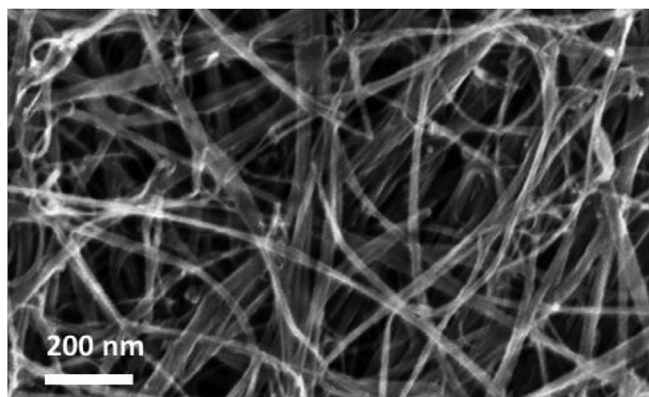


Fig. 11. SEM micrograph of as-received CNT veil ($\times 150,000$).

such as boron nitride nanotubes, as well as to systems where the Raman signal is not strong or obviously polarised, such as cellulose or other polymeric nanofibers.

Acknowledgement

The authors would like to thank Suzhou Institute of Nano-Tech and Nano-Bionics (Chinese Academy of Science) for their generosity of providing the carbon nanotube veils for this work. The authors would also like to thank Dr David Anthony and Ms Sandy Fisher for their discussions about composite characterisation and help with Raman spectroscopy, Dr Mahmoud Ardakani and Mrs Ecaterina Ware for their help with scanning electron microscopy, and Mr. Seigo Masuda and Dr Catriona McGilvery for their help with transmission electron microscopy.

The authors kindly acknowledge that funding for this research was provided by the UK Engineering and Physical Sciences Research Council (EPSRC).

Appendix A. Supplementary data

Supplementary data related to this article can be found at <https://doi.org/10.1016/j.carbon.2018.04.063>.

References

- [1] X.-L. Xie, Y.W. Ma, X.-P. Zhou, Dispersion and alignment of carbon nanotubes in polymer matrix: a review, *Mater. Sci. Eng. R Rep.* 49 (4) (2005) 89–112.
- [2] L. Hu, D.S. Hecht, G. Gruner, Carbon nanotube thin films: fabrication, properties, and applications, *Chem. Rev.* 110 (10) (2010) 5790–5844.
- [3] M.F.L. De Volder, S.H. Tawfik, R.H. Baughman, A.J. Hart, Carbon nanotubes: present and future commercial applications, *Science* 339 (2013) 535–539.
- [4] R. Downes, S. Wang, D. Haldane, A. Moench, R. Liang, Strain-induced alignment mechanisms of carbon nanotube networks, *Adv. Eng. Mater.* 17 (3) (2015) 349–358.
- [5] Z. Li, J.G. Park, Z. Liang, High-performance multifunctional thermoplastic composites enhanced by aligned buckypaper, *Adv. Eng. Mater.* 18 (8) (2016) 1460–1468.
- [6] Q.F. Cheng, J.P. Wang, J.J. Wen, C.H. Liu, K.L. Jiang, Q.Q. Li, S.S. Fan, Carbon nanotube/epoxy composites fabricated by resin transfer molding, *Carbon* 48 (1) (2010) 260–266.
- [7] Y. Han, X. Zhang, X. Yu, J. Zhao, S. Li, F. Liu, P. Gao, Y. Zhang, T. Zhao, Q. Li, Bio-inspired aggregation control of carbon nanotubes for ultra-strong composites, *Sci. Rep.* 5 (2015). Article number: 11533.
- [8] A.E. Aliev, C. Guthy, M. Zhang, S. Fang, A.A. Zakhidov, J.E. Fischer, R.H. Baughman, Thermal transport in MWCNT sheets and yarns, *Carbon* 45 (2007) 2880–2888.
- [9] L. Zhang, G. Zhang, C. Liu, S. Fan, High-density carbon nanotube buckypapers with superior transport and mechanical properties, *Nano Lett.* 12 (9) (2012) 4848–4852.
- [10] W. Feng, M. Qin, Y. Feng, Toward highly thermally conductive all-carbon composites: structure control, *Carbon* 109 (2016) 575–597.
- [11] T.S. Gspann, S.M. Junkes, J.F. Niven, M.B. Johnson, J.A. Elliot, M.A. White, A.H. Windle, High thermal conductivities of carbon nanotube films and micro-fibres and their dependence on morphology, *Carbon* 114 (2016) 160–168.
- [12] D. Wang, P. Song, C. Liu, W. Wu, S. Fan, Highly orientated carbon nanotube papers made of aligned carbon nanotubes, *Nanotechnology* 7 (2008), 075609.
- [13] M. Mecklenburg, D. Mizushima, N. Ohtake, W. Bauhofer, B. Fiedler, K. Schulte, On the manufacturing and electrical and mechanical properties of ultra-high wt.% fraction aligned MWCNT and randomly oriented CNT epoxy composites, *Carbon* 91 (2015) 275–290.
- [14] P. Liu, Y.F. Tan, D.C.M. Hu, D. Jewell, H.M. Duong, Multi-property enhancement of aligned carbon nanotube thin films from floating catalyst method, *Mater. Des.* 108 (2016) 754–760.
- [15] K. Koziol, J. Vilatela, A. Moisala, M. Motta, P. Cuniff, M. Sennett, A. Windle, High-performance carbon nanotube fiber, *Science* 318 (2007) 1892–1895.

- [16] T.H. Nam, K. Goto, K. Oshima, E.V.A. Premalal, Y. Shimamura, Y. Inoue, K. Naito, S. Ogiwara, Mechanical property enhancement of aligned multi-walled carbon nanotube sheets and composites through press-drawing process, *Adv. Compos. Mater.* 25 (1) (2016) 73–86.
- [17] W. Liu, X. Zhang, G. Xu, P.D. Bradford, X. Wang, H. Zhao, Y. Zhang, Q. Jia, F.G. Yuan, Q. Li, Y. Qiu, Y. Zhu, Producing superior composites by winding carbon nanotubes onto a mandrel under a poly(vinyl alcohol) spray, *Carbon* 49 (14) (2011) 4786–4791.
- [18] X. Wang, Z.Z. Yong, Q.W. Li, P.D. Bradford, W. Liu, D.S. Tucker, W. Cai, H. Wang, F.G. Yuan, Y.T. Zhu, Ultrastrong, stiff and multifunctional carbon nanotube composites, *Mater. Res. Lett.* 1 (1) (2013) 19–25.
- [19] J.H. Lehman, M. Mauricio Terrones, E. Mansfield, K.E. Hurst, V. Meunier, Evaluating the characteristics of multiwall carbon nanotubes, *Carbon* 49 (2011) 2581–2602.
- [20] T. Liu, S. Kumar, Quantitative characterization of SWNT orientation by polarized Raman spectroscopy, *Chem. Phys. Lett.* 378 (3) (2003) 257–262.
- [21] J.E. Fischer, W. Zhou, J. Vavro, M.C. Llaguno, C. Guthy, R. Haggenmueller, M.J. Casavant, D.E. Walters, R.E. Smalley, Magnetically aligned single wall carbon nanotube films: preferred orientation and anisotropic transport properties, *J. Appl. Phys.* 93 (4) (2003) 2157–2163.
- [22] C. Zamora-Ledezma, C. Blanc, M. Maugey, C. Zakri, P. Poulin, E. Anglaret, Anisotropic thin films of single-wall carbon nanotubes from aligned lyotropic nematic suspensions, *Nano Lett.* 8 (12) (2008) 4103–4107.
- [23] A.M. Rao, A. Jorio, M.S. Pimenta, S.S. Dantas, R. Saito, G. Dresselhaus, M.S. Dresselhaus, Polarized Raman study of aligned multiwalled carbon nanotubes, *Phys. Rev. Lett.* 84 (2000) 1820.
- [24] Weisstein, E. W. "Spherical Harmonic." From MathWorld—A Wolfram Web Resource. <http://mathworld.wolfram.com/SphericalHarmonic.html>.
- [25] Weisstein, E. W. "Legendre Polynomial." From MathWorld—A Wolfram Web Resource. <http://mathworld.wolfram.com/LegendrePolynomial.html>.
- [26] K.K. Kratmann, M.P.F. Sutcliffe, L.T. Lilleheden, R. Pyrz, O.T. Thomsen, A novel image analysis procedure for measuring fibre misalignment in unidirectional fibre composites, *Compos. Sci. Technol.* 69 (2) (2009) 228–238.
- [27] C.E. Ayres, G.L. Bowlin, B.S. Jha, H. Meredith, J.R. Bowman, S.C. Henderson, D.G. Simpson, Measuring fiber alignment in electrospun scaffolds: a user's guide to the 2d fast fourier transform approach, *J. Biomater. Sci. Polym. Ed.* 19 (5) (2008) 603–621.
- [28] M.J. Chow, R. Turcotte, C.P. Lin, Y. Zhang, Arterial extracellular matrix :a mechanobiological study of the contributions and interactions of elastin and collagen, *Biophys. J.* 106 (12) (2014) 2684–2692.
- [29] P. Thévenaz, M. Unser, User-friendly semiautomated assembly of accurate image mosaics in microscopy, *Microsc. Res. Tech.* 70 (2) (2007) 135–146.
- [30] R.C. Gonzalez, *Digital Image Processing*, Pearson Prentice Hall, Upper Saddle River, New Jersey, 2010. International of third edition.
- [31] Mathworkscom, Mathworkscom, Retrieved 28 November, 2016, from <https://uk.mathworks.com/help/matlab/ref/fft2.html>, , 2016.
- [32] Mathworkscom, Mathworkscom, Retrieved 28 November, 2016, from <https://uk.mathworks.com/help/matlab/ref/fftshift.html>, , 2016.
- [33] B. Osgood, Lecture notes for EE 261 the fourier transform and its applications, Retrieved 22 June 2017, <https://see.stanford.edu/materials/Isofaee261/book-fall-07.pdf>, 2007.
- [34] M. Zhao, B. Ming, J.W. Kim, L.J. Gibbons, X. Gu, T. Nguyen, C. Park, P.T. Lillehei, J.S. Villarrubia, A.E. Vladár, J. Alexander Liddle, New insights into subsurface imaging of carbon nanotubes in polymer composites via scanning electron microscopy, *Nanotechnology* 26 (16) (2015) 16901.
- [35] M.S. Dresselhaus, A. Jorio, A.G. Souza Filho, R. Saito, Defect characterization in graphene and carbon nanotubes using Raman spectroscopy, *Phil. Trans. R. Soc.* 368 (2010) 5355–5377.
- [36] A. Nakayama, S. Hoshino, Y. Yamada, A. Ohmura, F. Ishikawa, Counting graphene layers based on the light-shielding effect of Raman scattering from a substrate, *Appl. Phys. Lett.* 107 (2015), 231604.
- [37] R.Y. Zhang, Y. Wei, L.A. Nagahara, I. Amlani, R.K. Tsui, The contrast mechanism in low voltage scanning electron microscopy of single-walled carbon nanotubes, *Nanotechnology* 17 (2005) 1.
- [38] A. Vijayaraghavan, C. Marquardt, S. Dehm, F. Hennrich, R. Krupke, Imaging defects and junctions in single-walled carbon nanotubes by voltage-contrast scanning electron microscopy, *Carbon* 48 (2010) 2.